Influence of Untreated Metal Waste from 3D Printing on Electrical Properties of Alkali-Activated Slag Mortars

Lukáš Fiala [1,*], Michaela Petříková [1], Martin Keppert [1], Martin Böhm [1], Jaroslav Pokorný [2] and Robert Černý [1]

[1] Department of Materials Engineering and Chemistry, Faculty of Civil Engineering,
Czech Technical University in Prague, Thákurova 7/2077, 166 29 Prague, Czech Republic;
michaela.petrikova@fsv.cvut.cz (M.P.); martin.keppert@fsv.cvut.cz (M.K.); martin.bohm@fsv.cvut.cz (M.B.);
cernyr@fsv.cvut.cz (R.Č.)
[2] Department of Civil Engineering, Faculty of Technology, Institute of Technology and Business in České
Budějovice, Okružní 517/10, 370 01 České Budějovice, Czech Republic; jaroslav.pokorny@mail.vstecb.cz
* Correspondence: fialal@fsv.cvut.cz; Tel.: +420-2-2435-7125

Abstract: The negative environmental impact of cement production emphasizes the need to use alternative binders for construction materials. Alkali-activated slag is a more environmentally friendly candidate which can be utilized in the design of mortars with favorable material properties. However, the electrical properties of such materials are generally poor and need to be optimized by various metallic or carbon-based admixtures to gain new sophisticated material functions, such as self-sensing, self-heating, or energy harvesting. This paper investigates the influence of waste metal powder originating from the 3D printing process on the material properties of alkali-activated slag mortars. The untreated metal powder was characterized by means of XRD and SEM/EDS analyses revealing high nickel content, which was promising in terms of gaining self-heating function due to the high electrical conductivity and stability of nickel in a highly alkaline environment. The designed mortars with the waste metal admixture in the amount up to 250 wt.% to the slag and aggregates were then characterized in terms of basic physical, thermal, and electrical properties. Compared to the reference mortar, the designed mortars were of increased porosity of 17–32%. The thermal conductivity of ~1–1.1 W/m·K was at a favorable level for self-heating. However, the electrical conductivity of ~10^{-6} S/m was insufficient to allow the generation of the Joule heat. Even though a high amount of 3D printing waste could be used due to the good workability of mixtures, its additional treatment will be necessary to achieve reasonable, effective electrical conductivity of mortars resulting in self-heating function.

Keywords: alkali-activated slag mortar; 3D printing waste; electrical properties

1. Introduction

Alkali-activated slag mortars (AASMs) are composites based on ground-granulated blast-furnace slag (GGBFS), the precursor rich in CaO content (~35–40%) with latent hydraulicity. Hydration in relatively moderate alkaline compounds leads to the formation of calcium aluminate silicate hydrate [1] and calcium silicate hydrate gels, ensuring high mechanical strength [2]. Compared to cementitious mortars (CMs), AASMs are also of higher early age strength [1], higher chemical resistance [3], higher thermal stability [4], and a more environmentally friendly nature [5].

However, the electrical properties of AASMs (as well as those of CMs) are generally poor, and their insulative character does not allow new sophisticated functions usable in civil engineering applications, such as self-sensing, self-heating, or energy harvesting. The electrical conductivity of such materials ranges between ~10^{-9}–10^{-4} S/m [6–9], which is typical for electrical insulators. This shortcoming can be overcome by admixing electrically conductive admixtures (ECAs), which in certain dosages ensure significant improvement

in electrical properties of the doped composites. The influence of various ECAs on the effective electrical conductivity of the designed materials have been investigated in the past, mainly studied for cementitious materials, e.g., El-Dieb et al. [10] focused on steel shavings, carbon powder, and graphite powder that were used as a partial replacement of fine aggregates to reach favorable electrical properties. Belli et al. [11] focused on the optimization of high-conductive multifunctional fiber-reinforced cement mortars by using virgin carbon fibers, recycled carbon fibers, and brass-plated steel fibers, Berrocal et al. [12] studied the influence of steel fiber dosage and geometry on DC resistivity, and Wang and Aslani [13] comprehensively reviewed carbon-based and metallic ECAs and their effect on electrical properties of cementitious materials.

Taking into consideration the negative environmental impact of cement production: it is the third-largest source of anthropogenic emissions of CO_2 after fossil fuels and land use; more than 30 times increase of the global cement production since 1950; 1.5 ± 0.12 Gt estimated global CO_2 emissions in 2018; 38.3 ± 2.4 Gt the cumulative global CO_2 emissions between 1928 and 2018, of which 71% have occurred since 1990) [14], it is apparent that new construction materials based on binders with lower environmental impact should be designed and studied. Alkali-activated materials based on precursors from local sources can become, despite certain limitations [15], an alternative to cementitious composites due to competitive material properties and higher durability [16,17]. The design of multifunctional construction materials using waste/recycled ECAs to ensure favorable electrical properties may be a further step to decrease their environmental impact. Some efforts have already been made in cementitious materials [18,19], and such a trend can be expected in the field of alkali-activated aluminosilicate composites.

Since increasingly complex parts are required by various industries, 3D printing is an emerging manufacturing industrial field [20]. In addition to technologies for plastic 3D printing [21,22] with emphasis on reuse of plastic waste [23–25], metal 3D printing is important, e.g., for the automotive industry [26] or biomedical applications [27]. Metal 3D printing utilizes pure alloy powders or wires by two commonly used methods, powder bed fusion (PBF) and directed energy deposition (DED) [28], producing unfused waste powder from build jobs [29]. Despite such a powder is being often reused to reduce costs and the environmental impact of the manufacturing process; produced parts are of altered chemical composition and mechanical properties. Since the laser-powder interaction involves complex physics phenomena and generates byproducts affecting reused feedstock integrity, properties of parts built with reused powders are variable, even although similar starting alloys and process parameters are used [29].

The main objective of this paper was to characterize untreated waste metallic powder originating from the DED 3D printing process (M3DPWP) by XRD and SEM/EDS methods and verify its applicability as an admixture for AASMs, ensuring self-heating function. With respect to rapid development in metal 3D printing [20] and known issues [29], one can expect that new ways of reutilization of M3DPWP will be necessary for the future. With respect to results presented by Armoosh and Oltulu [30] and Zhang et al. [31], who observed a high-temperature increase of cementitious composites with particular metallic admixtures (copper, iron, and brass shavings in the amount up to 20%) under reasonable 60 V input voltage, and an outstanding self-heating ability of cementitious composites with nickel powder ensuring the temperature increase of about 50 °C at 20 V power input within 30 s of the experiment duration, respectively, M3DPWP is promising ECA from the point of view of self-heating ability.

2. Materials and Methods

The designed AASMs were based on ground-granulated GGBFS, three fractions of fine aggregates, sodium silicate activator-water glass (WG), and M3DPWP (Figure 1). Such a rich-on-nickel waste material was mainly used to adjust the electrical properties of mortars, which can bring new qualitative functions. Description of input materials is given in the following subsections.

Figure 1. Raw materials used for the design of AAMs with M3DPWP: (**a**) GGBFS; (**b**) WG; (**c**) M3DPWP; (**d**) aggregates.

2.1. Ground-Granulated Blast-Furnace Slag

GGBFS meeting ČSN EN 197-1 [32] was of 380 m^2/kg fineness with a dominant particle size in the range of 10–100 µm. Chemical composition and the particle size distribution (PSD) are presented in Table 1 and Figure 2.

Table 1. Chemical composition of GGBFS.

CaO (%)	SiO$_2$ (%)	Al$_2$O$_3$ (%)	MgO (%)	SO$_3$ (%)	MnO (%)	K$_2$O (%)	Fe$_2$O$_3$ (%)	TiO$_2$ (%)
39.14	36.62	10.84	10.17	1.67	0.41	0.41	0.31	0.28
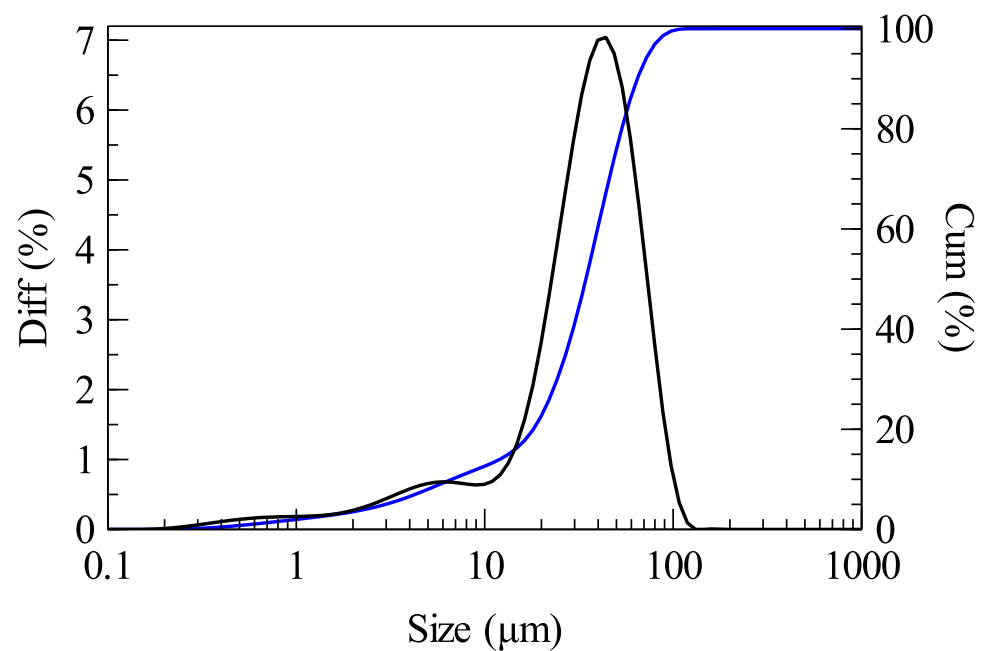
**Figure 2.** PSD of GGBFS.

2.2. Water Glass

GGBFS was alkali-activated by a solution of commercially produced sodium silicate (WG Britesil C205-Vodní Sklo a.s., Brno-jih, Czech Republic) with $SiO_2/Na_2O = 2.07$. The summary of important parameters and properties is given in Table 2.

Table 2. WG characterization (values declared by supplier Vodní sklo a.s.).

Parameter/Property	Declared	Measured
Molar ratio SiO_2/Na_2O (-)	1.95–2.15	2.07
SiO_2 (%)	51.60–55.40	53.75
Na_2O (%)	25.60–28.50	26.73
Bulk density (kg/m^3)	400–600	510
Loss on ignition–800 °C (%)	18.00–21.00	19.80
pH–10g/l H_2O, 20 °C (-)	11.5	-

2.3. Aggregates

Three normalized fractions of fine quartz of the size up to 4 mm were used in the ratio of 1:1:1 (Figure 3). Such natural, siliceous filler of high purity (>98% SiO_2) complying with ČSN EN 196-1 [33] standard originated from Chlum quarry (Filtrační písky, s.r.o., Chlum, Czech Republic).
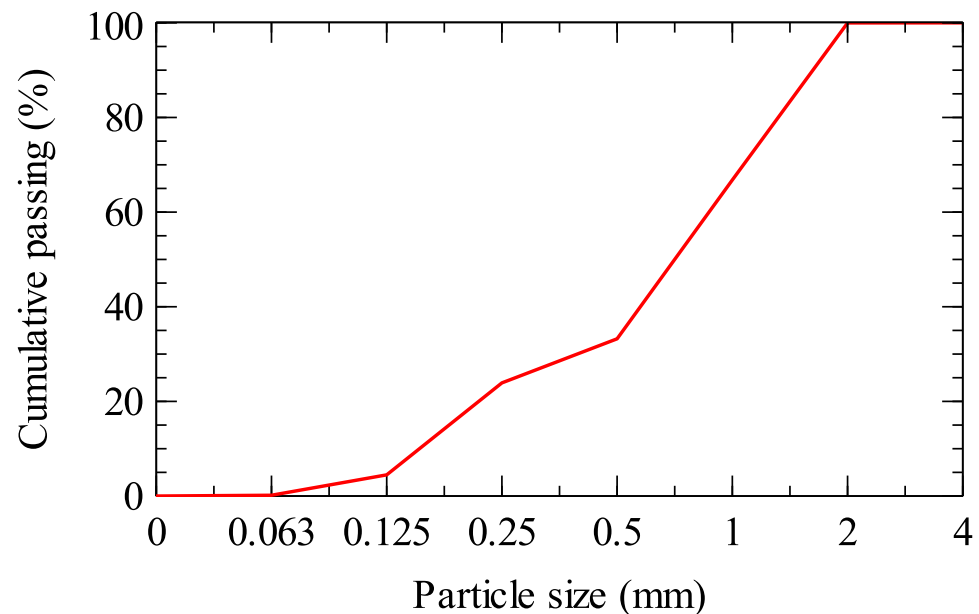
Figure 3. PSD of aggregates.

2.4. 3D Printing Waste

M3DPWP was delivered by the Czech producer of precise 3D components for automotive (COMTES FHT a.s.). The waste powder originated from an additive production of 3D parts with high-quality requirements on the InssTek MX600 device. The production is based on Direct Energy Deposition (DED) technology: The raw metal powder is supplied to the focus of the laser beam in a higher quantity than needed to form the weld, and excess powder is dispersed in the working space of the deposition equipment. The whole printing process is performed under the protection of argon atmosphere, which the heated excess powder leaves. Without the protection of argon atmosphere, hot powder particles oxidize, and due to the high-quality requirements of 3D parts, such excess powder is not reutilized in 3D printing.

The waste powder is typically a mix of the following (oxidized) alloys: Fe alloys (316L, SAF2507, 1.2709, 431L, P21), Ni alloys (IN718, Nimonic 80A, Hastelloy C22), Co alloys (Stellite 6, Stellite 21, CoCrMo), or Ti alloys (CP Ti Grade 1, Ti6Al4V Grade 5, Ti5Al5Mo5V3Cr). The particle size of the used powders is typically in the range of 45–150 μm, or optionally in narrower fractions, e.g., 45–106 μm or 80–120 μm. Recycling the waste powder is possible by removing oxidized particles and agglomerates. Despite the treated waste can be mixed with corresponding raw powder of the same composition and reused, even very

low contamination with residues of other alloy-powders used for 3D printing of different components is limiting due to the high-quality demands of the final 3D-printed products.

2.5. Mixing Procedure

The composition of AAM mixtures is given in Table 3. They were prepared using the following procedure. First, an alkaline activator solution was prepared by dissolving WG in water. Contrary to the preparation of alkali-activated slag with carbon-based admixtures, where ECA is added in the form of suspension [9], M3DPWP was mixed directly with GGBFS. GGBFS with M3DPWP was then mixed with the prepared WG solution for 2 min. Three fractions of aggregates were added to the mixture and mixed again for 5 min. Mixtures were then put into molds and compacted by vibration. After 24 h, solidified samples were unmolded and cured for 27 days in a water bath. Samples were then dried in an oven and cooled in a desiccator to avoid the sorption of water vapor before forthcoming experimental investigations.

Table 3. Composition of AAMs.

Component	M1	M2	M3	M4	M5
GGBFS (g)	100	100	100	100	100
WG (g)	20	20	20	20	20
Aggregates (g)	300	300	300	300	300
M3DPWP (g)	0	30	200	600	1000
Water/GGBFS ratio (-)	0.44	0.47	0.47	0.67	1.11

2.6. XRF and SEM Analysis

The elemental composition of the entire material was estimated by a handheld EDXRF spectrometer. The phase composition of metal particles that were placed freely on a nondiffracting silicon plate was examined by a PANalytical Aeris diffractometer equipped with a CoKα tube operating at 40 kV and 7.5 mA. The incident beam path consisted of iron beta-filter, Soller slits 0.04 rad and divergence slit $1/2°$, the diffracted beam path was equipped with 9 mm anti-scatter slit, and Soller slits 0.04 rad. The detector PIXcel1D-Medipix3 of $5.542°$ active length was used, and the measured data were evaluated by Profex 4.0.3 [34]. The SEM micrographs were acquired using Phenom XL microscope operating with BSE detector at 15 kV accelerating voltage, and the composition of individual particles was examined by EDS spectra recorded by the SEM device.

2.7. Basic Physical Properties

Basic physical properties were represented by the bulk density ρ_v (kg/m^3), the matrix density ρ_{mat} (kg/m^3), and the total open porosity Ψ (%). The bulk density of mortars was determined on three dried 50 mm $\times$ 50 mm $\times$ 50 mm samples by the gravimetric method according to ČSN EN 1015-10 standard [35], the matrix density of mortars and the density of M3DPWP were determined by the helium pycnometry (Pycnomatic ATC device), and the total open porosity was calculated with respect to ρ_v and ρ_{mat} data.

2.8. Thermal Properties

The thermal conductivity and the specific heat capacity were determined by ISOMET 2114 device (Figure 4). Non-steady state measurements were carried out on 70 mm $\times$ 70 mm $\times$ 70 mm samples by IPS 1105 surface probe providing a sufficient measuring range of the thermal conductivity and volumetric heat capacity of 0.03–6 W/m·K, and $4 \cdot 10^4$–$3 \cdot 10^6$ J/m^3·K, respectively.

Figure 4. ISOMET 2114 device.

2.9. Electrical Properties

Electrical properties were determined on 50 mm × 50 mm × 50 mm samples attached with two-layered carbon paint and copper adhesive paste in direct current (DC) and alternate current (AC) regime (Figure 5a). DC measurements were performed using a precise Fluke 8846A multimeter. The effective electrical conductivity σ (S/m) of mortars was calculated with respect to the average of ~100 measured resistance values R (Ω), the area of electrodes S (m^2), and the distance between electrodes l (m) according to Equation (1),

$$\sigma = \frac{1}{R} \cdot \frac{l}{S} \tag{1}$$
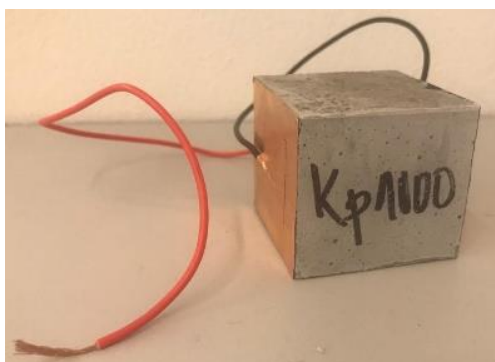
(**a**)
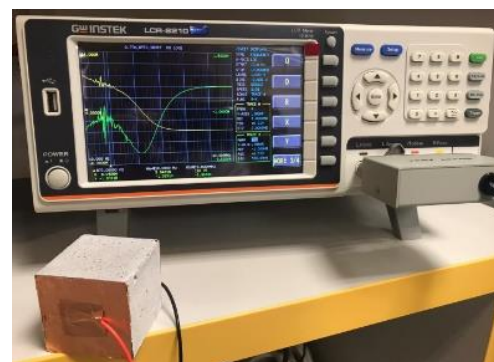
(**b**)

Figure 5. (**a**) Sample attached by electrodes; (**b**) LCR bridge for measurements of AC electrical properties.

AC electrical properties, represented by the magnitude of impedance $|Z|$ (Ω) and the phase shift θ (°), were determined on 50 mm × 50 mm × 50 mm samples by a precise LCR bridge (GWInstek LCR-8210) with the measuring range up to 10 MHz (Figure 5b).

3. Results and Discussion

The density of M3DPWP determined by the helium pycnometry was ρ = 8172 kg/m^3. The results of the elemental analysis of metal particles are presented in Figure 6. Ni was present at the highest amount (36.4%); other significant metals were Fe (~20%), Cr (~20%), and Co (~15%). Traces of Ti, Mo, Nb, W, Mn, and Al were also observed.
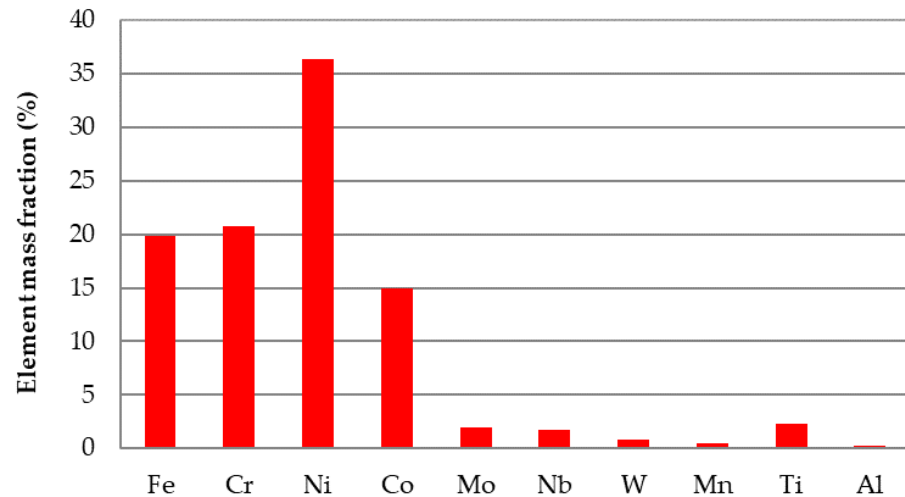

Figure 6. Composition of M3DPWP.

The SEM micrography revealed the presence of three types of visually distinguishable particles (Figure 7a) with the composition estimated by EDS spectroscopy (Figure 8). It also indicated oxygen in EDS spectra as the result of surface passivation and a small amount of carbon, most likely due to the surface contamination. Since the main goal lay in the description of the nature of metal particles, oxygen and carbon were not taken into consideration in EDS spectra evaluation. Ni was the dominant metal of the spherical particles labeled as A; the other components were Cr, Fe, Mo, Nb, and traces of Ti and Al (Figure 8). The composition corresponded to the "Inconel alloys" family (Inconel IN718). Particles labeled as B were rich in Fe and Cr and corresponded to the "duplex stainless steel" family (SAF2507), while particles labeled as C were rich in cobalt alloy from the "Stellite" family (Stellite 6), also containing Cr, W and a small amount of Fe. Unlike the "Inconel" and "duplex stainless steel," Stellites contained a few percent of carbon, but EDS obviously did not enable us to distinguish the carbon being the part of alloy and that coming from contamination. Thus, the C was again excluded from the EDS data, even though, in this case, C is a component of the alloy.
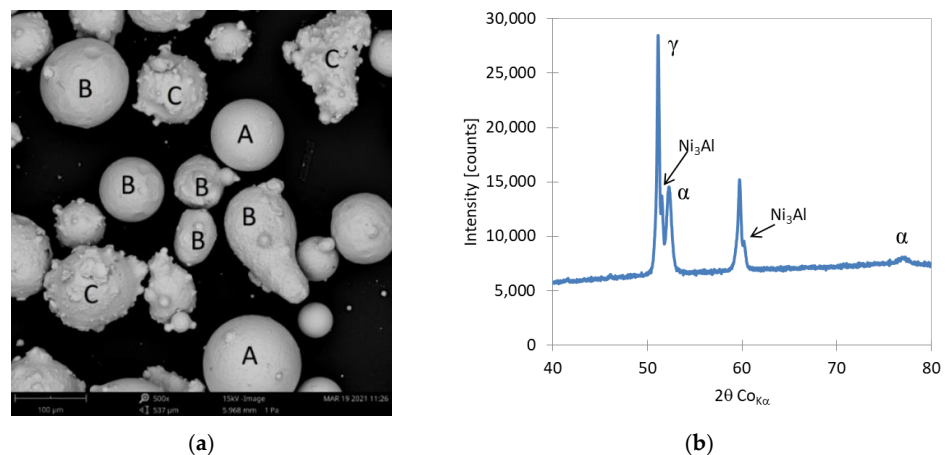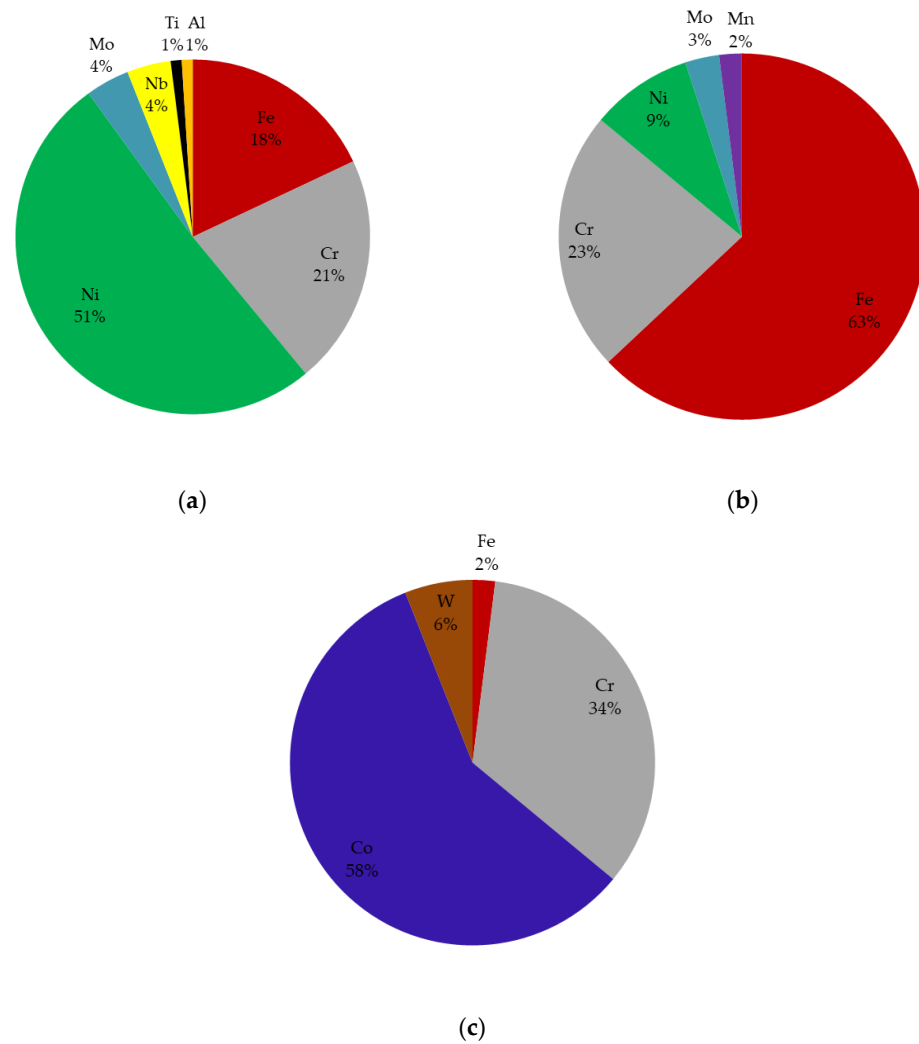

(a)

(b)

Figure 7. (**a**) SEM image of metal particles; (**b**) X-ray diffractogram of metal particles: α—bcc phases; γ—fcc phases.

(a)

(b)

(c)

Figure 8. Composition of metal particles (EDS spectroscopy). (**a**) A-type particle; (**b**) B-type particle; (**c**) C-type particle.

The X-ray diffractogram of metal particles is presented in Figure 7b. It contained two distinct diffractions labeled as α and γ; the latter one belongs to austenitic phases (fcc), which were present in all three types of particles: Inconel (A), duplex stainless steel (B), and Stellite (C). The duplex stainless steel (B) also contained ferritic phase (bcc) labeled as α in XRD. The last distinct phase was most likely Ni3Al, present in Inconel as an "austenite stabilizer."

The size and shape of M3DPWP particles were determined on the basis of SEM image analysis (6 images, approx. 300 objects). In Figure 9, an example of one processed image and length-, width-, circularity histograms are given. Particles were dominantly 50–150 μm in size and exhibited highly circular shape (high proportion of particles of 0.7–1 circularity).
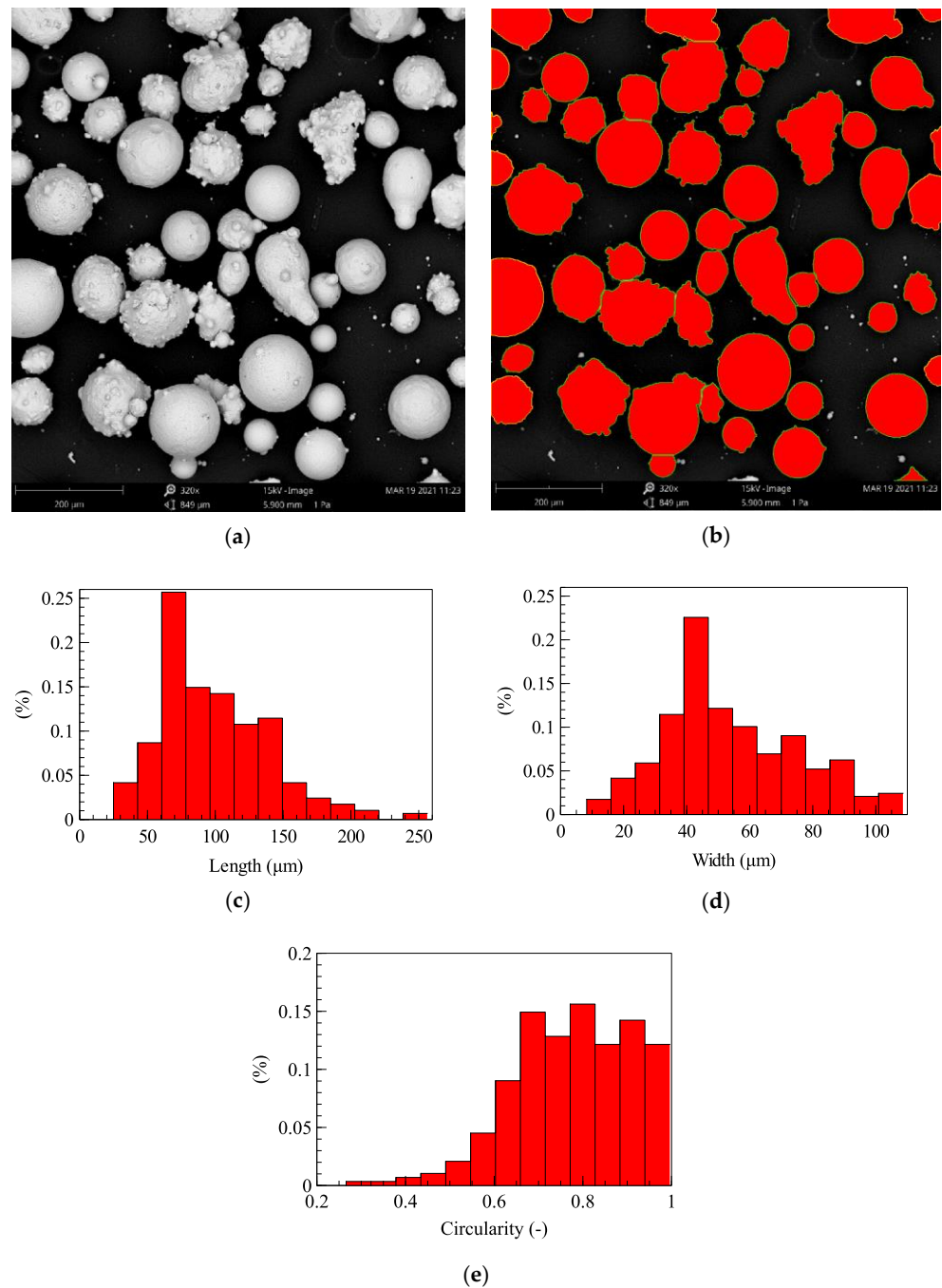
Figure 9. Size and shape characterization of 3D printing metal waste. (**a**) SEM image; (**b**) SEM image ready for characterization; (**c**) Histogram of particle length distribution; (**d**) Histogram of particle width distribution; (**e**) Histogram of particle circularity distribution.

The basic physical properties of the designed mixtures are summarized in Figure 10. The reference mortar M1 exhibited the lowest bulk/matrix density, and the total open porosity (ρ_v = 2130 kg/m^3, ρ_{mat} = 2556 kg/m^3, Ψ = 16.7%). With the increasing amount of M3DPWP ρ_v, ρ_{mat}, Ψ increased. The highest values ρ_v = 3518 kg/m^3, ρ_{mat} = 5162 kg/m^3, Ψ = 31.8% were observed for M5 mortar. The presence of metal waste significantly influenced the formation of a highly porous structure compared to the reference mortar; the porosity increased from ~17% to 32%.
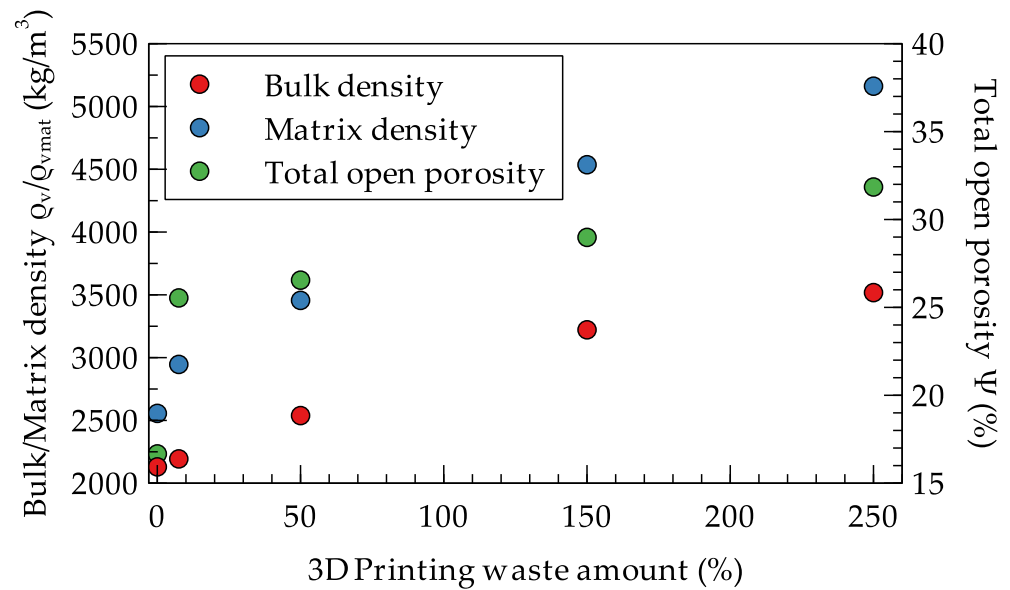
Figure 10. Bulk/matrix density, total open porosity.

A decreasing trend of the thermal conductivity was observed with increasing dosage of metal waste (Figure 11), the highest value was observed for M1 (λ = 1.36 W/m·K), whereas the lowest for M5 (0.75 W/m·K). Thermal conductivity was influenced by two contradictory phenomena; the increasing total open porosity corresponding with an increasing amount of M3DPWP related with the unfavorable interfacial transition zone between aluminosilicate matrix and metal waste was more significant than an increasing amount of metal waste with high thermal conductivity. The specific heat capacity (Figure 12) exhibited a decreasing tendency with an increasing amount of M3DPWP from 773 J/kg·K (M1) to 460 J/kg·K (M5), which corresponds with specific heat capacities of involved components (aluminosilicate binder and metallic admixture).
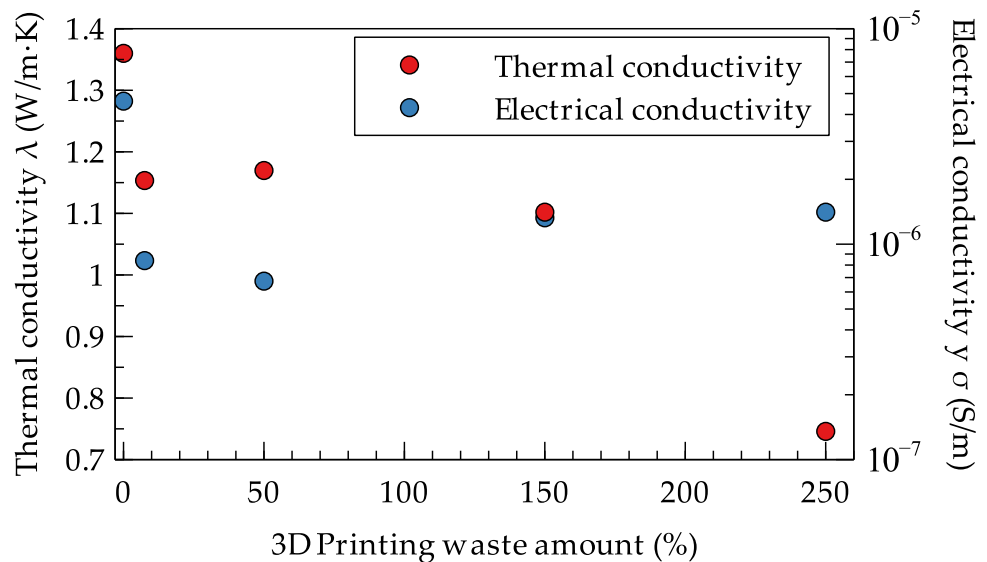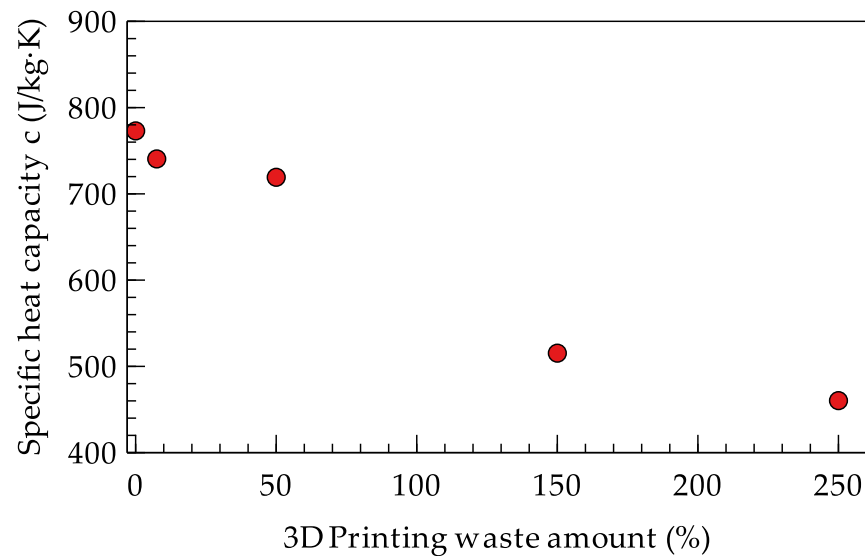

**Figure 11.** Thermal and electrical conductivity.

Figure 12. Specific heat capacity.

The electrical conductivity did not exhibit the expected increasing trend with increasing the dosage of M3DPWP (Figure 11). The highest electrical conductivity was observed for the reference mortar M1 ($\sigma = 4.61 \times 10^{-6}$ S/m), which can be mainly explained by a compact aluminosilicate matrix (low porosity) containing some conductive paths formed by the residual amount of iron in GGBFS [36]. A slight decrease in electrical conductivity observed up to 50 wt.% of M3DPWP was followed by a slight increase at higher dosages (150 and 250 wt.%). In general, the electrical conductivity of M2-M5 was ~10^{-6} S/m.

The expected increase in the electrical conductivity of mortars with M3DPWP was not mainly achieved thanks to the following aspects: (1) utilization of oxidized metal particles. During the 3D printing process, the metal particles heated to high temperatures left the protective argon atmosphere, reacted with oxygen, which resulted in the formation of a surface NiO layer [37]. NiO was of much lower electrical conductivity (~10^{-8} S/m [38]) compared to pure nickel (~10^6 S/m). (2) High alkali environment of fresh AASMs led to the formation of β-Ni(OH)$_2$ [39] with the electrical conductivity of ~10^{-2} S/m [40]. Passivation effect was also important in the case of steel alloys, which was published, e.g., by Wang et al. [41], who focused on corrosion of steel bars immersed in simulated pore solutions of AASM. Thanks to the passivation effects of M3DPWP compounds, the effective electrical conductivity of mortars was not significantly increased to the level required for self-heating function [9].

In Figure 13, the magnitude of impedance/the phase shift dependencies on the frequency of the designed mortars are given. In general, the reasonably low magnitude of impedance and phase shift close to 0° indicate the resistive character of materials which is a crucial assumption for self-heating ability. For all the studied composites, the magnitude of impedance was in the range of 10^7–10^8 Ω at low frequencies and significantly decreased by 3–5 orders of magnitude with increasing frequency which is typical for materials of the capacitive character. This character was confirmed by the phase shift dependence on a frequency that decreased from -5–$-20°$ (low frequencies) to ~$-85°$ (10 MHz). The results revealed behavior that is typical for heterogeneous materials without a well-formed electrically conductive net within the solid matrix. Results of AC measurements were in accordance with observations for DC measurements.
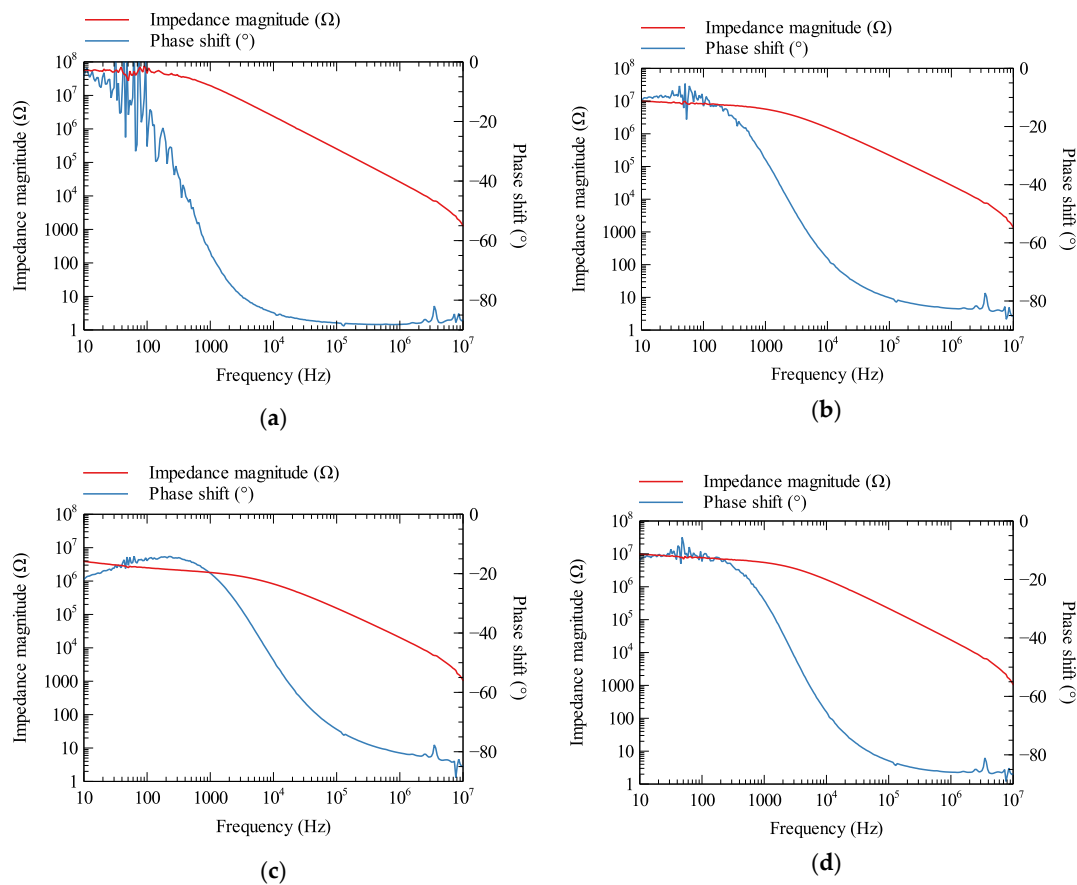
Figure 13. AC electrical properties: impedance magnitude/phase shift dependencies on the frequency. (**a**) M2; (**b**) M3; (**c**) M4; (**d**) M5.

4. Conclusions

Metallic waste originating from 3D printing with a declared significant amount of Ni was used as a promising filler for the design of AASMs with optimized electrical properties. The waste was characterized in terms of composition and particle size distribution. Mortars with various dosages of M3DPWP up to 250 wt.% were prepared and characterized in terms of basic physical, thermal, and electrical properties, which are important for the assessment of their self-heating ability.

Based on observation, the following conclusions were drawn:

- The amount of Ni in M3DPWP was 36.4%.
- Three types of visually distinguishable particles were observed in M3DPWP, A-type particles were rich in Ni, B-type particles on Fe, and C-type particles on Co, which corresponded with alloys used in 3D build jobs: Inconel IN718, SAF2507, and Stellite.
- M3DPWP particles were dominantly 50–150 μm in size and a circular shape (high proportion of particles of 0.7–1 circularity).
- M3DPWP increased the porosity of AASMs by 17–32%. The porosity increase was directly proportional to the amount of M3DPWP.
- The thermal conductivity of AASMs was influenced positively by the high thermal conductivity of the involved M3DPWP and negatively by the porosity. It remained at a reasonable level of ~1.15 W/m·K, allowing self-heating function up to 150 wt.% of M3DPWP.
- The specific heat capacity of AASMs systematically decreased with increasing M3DPWP amount.
- Addition of M3DPWP did not enhance the DC electrical conductivity of AASMs to the level ensuring self-heating function. It could be mainly due to passivation layers formed by NiO (cooling of M3DPWP out of the protective argon atmosphere) and

β-Ni(OH)$_2$ (alkali environment in fresh AASMs). Both NiO and β-Ni(OH)$_2$ are of significantly lower electrical conductivity (10^{-6} and 10^{-2} S/m) than pure Ni (10^6 S/m). Therefore, even though a high amount of M3DPWP allowed the forming of paths, they we not sufficiently electrically conductive to evolve the Joule heat under the voltage load.

- AC electrical measurements revealed the capacitive character of AASMs with M3DPWP, which was unfavorable in terms of self-heating function in the AC electric field.
- Although the self-heating function of the designed AASMs was not achieved even at high M3DPWP dosages, treatment of M3DPWP after 3D printing/before admixing to AASMs can lead to the higher effective electrical conductivity of AASMs thanks to the removal of low electrically conductive NiO passivation layer and formation of higher electrically conductive β-Ni(OH)$_2$. Such an assumption needs to be further experimentally verified.

Institutional Review Board Statement: Not applicable.

Informed Consent Statement: Not applicable.

Data Availability Statement: The data presented in this study are available on request from the corresponding author.

Conflicts of Interest: The authors declare no conflict of interest.

References

1. Palomo, A.; Krivenko, P.; Garcia-Lodeiro, I.; Kavalerova, E.; Maltseva, O.; Fernandét-Jiménez, A. A review on alkaline activation: New analytical perspectives. *Mater. Constr.* **2014**, *64*, e022. [CrossRef]
2. Alonso, M.M.; Gismera, S.; Blanco, M.T.; Lanzón, M.; Puertas, F. Alkali-activated mortars: Workability and rheological behaviour. *Constr. Build. Mater.* **2017**, *145*, 576–587. [CrossRef]
3. Criado, M.; Provis, J.L. Alkali Activated Slag Mortars Provide High Resistance to Chloride-Induced Corrosion of Steel. *Front. Mater.* **2018**, *5*, 34. [CrossRef]
4. Zuda, L.; Pavlík, Z.; Rovnaníková, P.; Bayer, P.; Černý, R. Properties of Alkali Activated Aluminosilicate Material after Thermal Load. *Int. J. Thermophys.* **2006**, *27*, 1250–1263. [CrossRef]
5. Ameri, F.; Zareei, S.A.; Behforouz, B. Zero-cement vs. cementitious mortars: An experimental comparative study on engineering and environmental properties. *J. Build. Eng.* **2020**, *32*, 101620. [CrossRef]
6. Monfore, G.E. The electrical resistivity of concrete. *J. PCA Res. Dev. Lab.* **1968**, *10*, 35–48.
7. Whittington, H.W.; McCarter, J.; Forde, M.C. The conduction of electricity through concrete. *Mag. Concr. Res.* **1981**, *33*, 48–60. [CrossRef]
8. Xie, P.; Gu, P.; Beaudoin, J.J. Electrical percolation phenomena in cement composites containing conductive fibres. *J. Mater. Sci.* **1996**, *31*, 4093–4097. [CrossRef]
9. Fiala, L.; Petříková, M.; Lin, W.-T.; Podolka, L.; Černý, R. Self-Heating Ability of Geopolymers Enhanced by Carbon Black Admixtures at Different Voltage Loads. *Energies* **2019**, *12*, 4121. [CrossRef]
10. El-Dieb, A.S.; El-Ghareeb, M.A.; Abdel-Rahman, M.A.H.; Nasr, E.S.A. Multifunctional electrically conductive concrete using different fillers. *J. Build. Eng.* **2018**, *15*, 61–69. [CrossRef]
11. Belli, A.; Mobili, A.; Bellezze, T.; Tittarelli, F. Commercial and recycled carbon/steel fibers for fiber-reinforced cement mortars with high electrical conductivity. *Cem. Concr. Compos.* **2020**, *109*, 103569. [CrossRef]
12. Berrocal, C.G.; Hornbostel, K.; Geiker, M.R.; Löfgren, I.; Lundgren, K.; Bekas, D.G. Electrical resistivity measurements in steel fibre reinforced cementitious materials. *Cem. Concr. Compos.* **2018**, *89*, 216–229. [CrossRef]
13. Wang, L.; Aslani, F. A review on material design, performance, and practical application of electrically conductive cementitious composites. *Constr. Build. Mater.* **2019**, *229*, 116892. [CrossRef]
14. Andrew, R.M. Global CO$_2$ emissions from cement production 1928–2018. *Earth Syst. Sci. Data* **2019**, *11*, 1675–1710. [CrossRef]

15. Assi, L.N.; Carter, K.; Deaver, E.; Ziehl, P. Review of availability of source materials for geopolymer/sustainable concrete. *J. Clean. Prod.* **2020**, *263*, 121477. [CrossRef]
16. Rakhimova, N.R. Recent advances in blended alkali-activated cements: A review. *Eur. J. Environ. Civ. Eng.* **2020**. early access. [CrossRef]
17. Wang, A.; Zheng, Y.; Zhang, Z.; Liu, K.; Li, Y.; Shi, L.; Sun, D. The Durability of Alkali-Activated Materials in Comparison with Ordinary Portland Cements and Concretes: A Review. *Engineering* **2020**, *6*, 695–706. [CrossRef]
18. Deghanpour, H.; Yilmaz, K. A more sustainable approach for producing less expensive electrically conductive concrete mixtures: Experimental and FE study. *Cold Reg. Sci. Technol.* **2021**, *184*, 103231. [CrossRef]
19. Norambuena-Contreras, A.J.; Quilodran, J.; Gonzales-Torre, I.; Chavez, M.; Borinaga-Trevino, R. Electrical and thermal characterisation of cement-based mortars containing recycled metallic waste. *J. Clean. Prod.* **2018**, *190*, 737–751. [CrossRef]
20. Ngo, T.D.; Kashani, A.; Imbalzano, G.; Nguyen, K.T.Q.; Hui, D. Additive manufacturing (3D printing): A review of materials, methods, applications and challenges. *Compos. Part B* **2018**, *143*, 172–196. [CrossRef]
21. Skoratko, A.; Katzer, J. Harnessing 3D Printing of Plastics in Construction—Opportunities and Limitations. *Materials* **2021**, *14*, 4547. [CrossRef]
22. Chae, M.P.; Rozeni, W.M.; McMenamin, P.G.; Findlay, M.W.; Spychal, R.T.; Hunter-Smith, D.J. Emerging applications of bedside 3D printing in plastic surgery. *Front. Surg.* **2015**, *2*, 25. [CrossRef]
23. Kantaros, A.; Laskaris, N.; Piromalis, D.; Ganetsos, T. Manufacturing Zero-Waste COVID-19 Personal Protection Equipment: A Case Study of Utilizing 3D Printing While Employing Waste Material Recycling. *Circ. Econ. Environ. Prot.* **2021**, *1*, 851–869.
24. Woern, A.L.; Byard, D.J.; Oakley, R.B.; Fiedler, M.J.; Snabes, S.L.; Pearce, J.M. Fused Particle Fabrication 3-D Printing: Recycled Materials' Optimization and Mechanical Properties. *Materials* **2018**, *11*, 1413. [CrossRef] [PubMed]
25. Woern, A.L.; McCaslin, J.R.; Pringle, A.M.; Pearce, J.M. RepRapable Recyclebot: Open source 3-D printable extruder for converting plastic to 3-D printing filament. *Hardwarex* **2018**, *4*, e00026. [CrossRef]
26. Mahmood, M.A.; Popescu, A.C.; Mihailescu, I.N. Metal Matrix Composites Synthesized by Laser-Melting Deposition: A Review. *Materials* **2020**, *13*, 2593. [CrossRef]
27. Velasquez-Garcia, L.F.; Kornbluth, Y. Biomedical Applications of Metal 3D Printing. *Annu. Rev. Biomed. Eng.* **2021**, *23*, 307–338. [CrossRef]
28. Gadagi, B.; Lekurwale, R. A review on advances in 3D metal printing. *Mater. Today Proc.* **2021**, *45*, 277–283. [CrossRef]
29. Santecchia, E.; Spigarelli, S.; Cabibbo, M. Material Reuse in Laser Powder Bed Fusion: Side Effects of the Laser—Metal Powder Interaction. *Metals* **2020**, *10*, 341. [CrossRef]
30. Armoosh, S.R.; Oltulu, M. Self-heating of electrically conductive metal-cementitious composites. *J. Intell. Mater. Syst. Struct.* **2019**, *30*, 2234–2240. [CrossRef]
31. Zhang, K.; Han, B.; Yu, X. Nickel particle based electrical resistance heating cementitious composites. *Cold Reg. Sci. Technol.* **2011**, *69*, 64–69. [CrossRef]
32. *ČSN EN 197-1, Cement—Part 1: Composition, Specifications and Conformity Criteria for Common Cements*; Czech Office for Standards, Metrology and Testing: Prague, Czech Republic, 2001.
33. Czech Office for Standards, Metrology and Testing. *ČSN EN 196-1, Methods of Testing Cement—Part 1: Determination of Strength*; Czech Office for Standards, Metrology and Testing: Prague, Czech Republic, 2016.
34. Döbelin, N.; Kleeberg, R. Profex: A graphical user interface for the Rietveld refinement program BGMN. *J. Appl. Crystallogr.* **2015**, *48*, 1573–1580. [CrossRef] [PubMed]
35. Czech Office for Standards, Metrology and Testing. *ČSN EN 1015-10, Methods of Test for Mortar for Masonry—Part 10: Determination of Dry Bulk Density of Hardened Mortar*; Czech Office for Standards, Metrology and Testing: Prague, Czech Republic, 2000.
36. Rovnaník, P.; Kusák, I.; Bayer, P.; Schmid, P.; Fiala, L. Comparison of electrical and self-sensing properties of Portland cement and alkali-activated slag mortars. *Cem. Concr. Res.* **2019**, *118*, 84–91. [CrossRef]
37. Haugsrud, R. On the high-temperature oxidation of nickel. *Corros. Sci.* **2003**, *45*, 211–235. [CrossRef]
38. Morin, F.J. Electrical Properties of NiO. *Phys. Rev.* **1954**, *93*, 1199–1204. [CrossRef]
39. Wang, Z.H.; Lu, Y.H.; Li, J.; Shoji, T. Effect of pH value on the fretting wear behavior of Inconel 690 alloy. *Tribol. Int.* **2016**, *95*, 162–169. [CrossRef]
40. Hall, D.S.; Lockwood, D.J.; Bock, C.; MacDougall, B.R. Nickel hydroxides and related materials: A review of their structures, synthesis and properties. *Proc. R. Soc. A Math. Phys. Eng. Sci.* **2015**, *471*, 20140792. [CrossRef] [PubMed]
41. Wang, W.; Chen, H.; Li, X.; Zhu, Z. Corrosion behavior of steel bars immersed in simulated pore solutions of alkali-activated slag mortar. *Constr. Build. Mater.* **2017**, *143*, 289–297. [CrossRef]